RESEARCH ARTICLE

National Science Review
5: 70–77, 2018
doi: 10.1093/nsr/nwx051
Advance access publication 2 May 2017

MATERIALS SCIENCE

Three-dimensional artificial transpiration for efficient solar waste-water treatment

Xiuqiang Li[1], Renxing Lin[1], George Ni[2], Ning Xu[1], Xiaozhen Hu[1], Bin Zhu[1], Guangxin Lv[1], Jinlei Li[1], Shining Zhu[1] and Jia Zhu[1,*]

ABSTRACT

Solar steam generation is emerging as promising solar-energy conversion technology for potential applications in desalination, sterilization and chemical purification. Despite the recent use of photon management and thermal insulation, achieving optimum solar steam efficiency requires simultaneous minimization of radiation, convection and conduction losses without compromising light absorption. Inspired by the natural transpiration process in plants, here we report a 3D artificial transpiration device with all three components of heat loss and angular dependence of light absorption minimized, which enables over 85% solar steam efficiency under one sun without external optical or thermal management. It is also demonstrated that this artificial transpiration device can provide a complementary path for waste-water treatment with a minimal carbon footprint, recycling valuable heavy metals and producing purified water directly from waste water contaminated with heavy metal ions.

Keywords: graphene, solar vapor, heat loss, waste water, heavy-metal ions, water purification

[1]National Laboratory of Solid State Microstructures, College of Engineering and Applied Sciences, School of Physics, and Collaborative Innovation Center of Advanced Microstructures, Nanjing University, Nanjing 210093, China and [2]Department of Mechanical Engineering, Massachusetts Institute of Technology, Cambridge, Massachusetts 02139, USA

*Corresponding author. E-mail: jiazhu@nju.edu.cn

Received 5 March 2017; **Revised** 19 April 2017; **Accepted** 19 April 2017

INTRODUCTION

Recently, solar steam and vapor generation [1–13] have been attracting attention for their promising prospects in the fields of desalination, sterilization and chemical purification [14–21]. In the process of solar steam and vapor generation, there are several outlets for the input solar energy: total enthalpy of the liquid–vapor phase change (sensible heat and phase-change enthalpy), optical losses (including reflection and transmission of light) and thermal losses (including radiation, convection and conduction losses) (Fig. 1a). Impressive progress in the development of light absorbers [1–6,14–18] have led to minimized optical losses. Various heat localization techniques [7–13,19–21] such as thermal concentration [10] and confined water supply [21] have also been developed to minimize heat conduction losses without compromising water supply. With maximized solar-energy input (because of minimized optical losses) and minimized heat conduction losses, radiation and convection losses start to dominate as the absorber temperatures elevate. So far, high efficiencies (∼80%) have been achieved, but only by relying on thermal insulation [6,8,13] and/or optical concentration [3,7,15]. Therefore, efficient solar vapor generation under normal one sun illumination without extra thermal or optical supporting systems will fundamentally improve the scalability and economics of solar vapor generation.

Conveniently, nature already provides an elegant solution for efficient evaporation. In the transpiration processes of plants, water is pumped up from the roots and carried along a confined path up to leaves, achieving efficient water supply and evaporation [22,23]. In addition, the natural 3D structures of plants maximize light absorption from a wide range of incident angles throughout the day. Inspired by this transpiration process and 3D morphology of plants, we demonstrate a 3D artificial transpiration device, composed of a 3D hollow cone absorber connected with a 1D water path, as shown in Fig. 1b (scanning electron microscopy (SEM) images of each part are shown in Fig. 1c–e. More details about the morphology of graphene oxide (GO) film are included in Supplemental S1, available as Supplementary Data at *NSR* online). During the artificial transpiration process, water is taken up by a

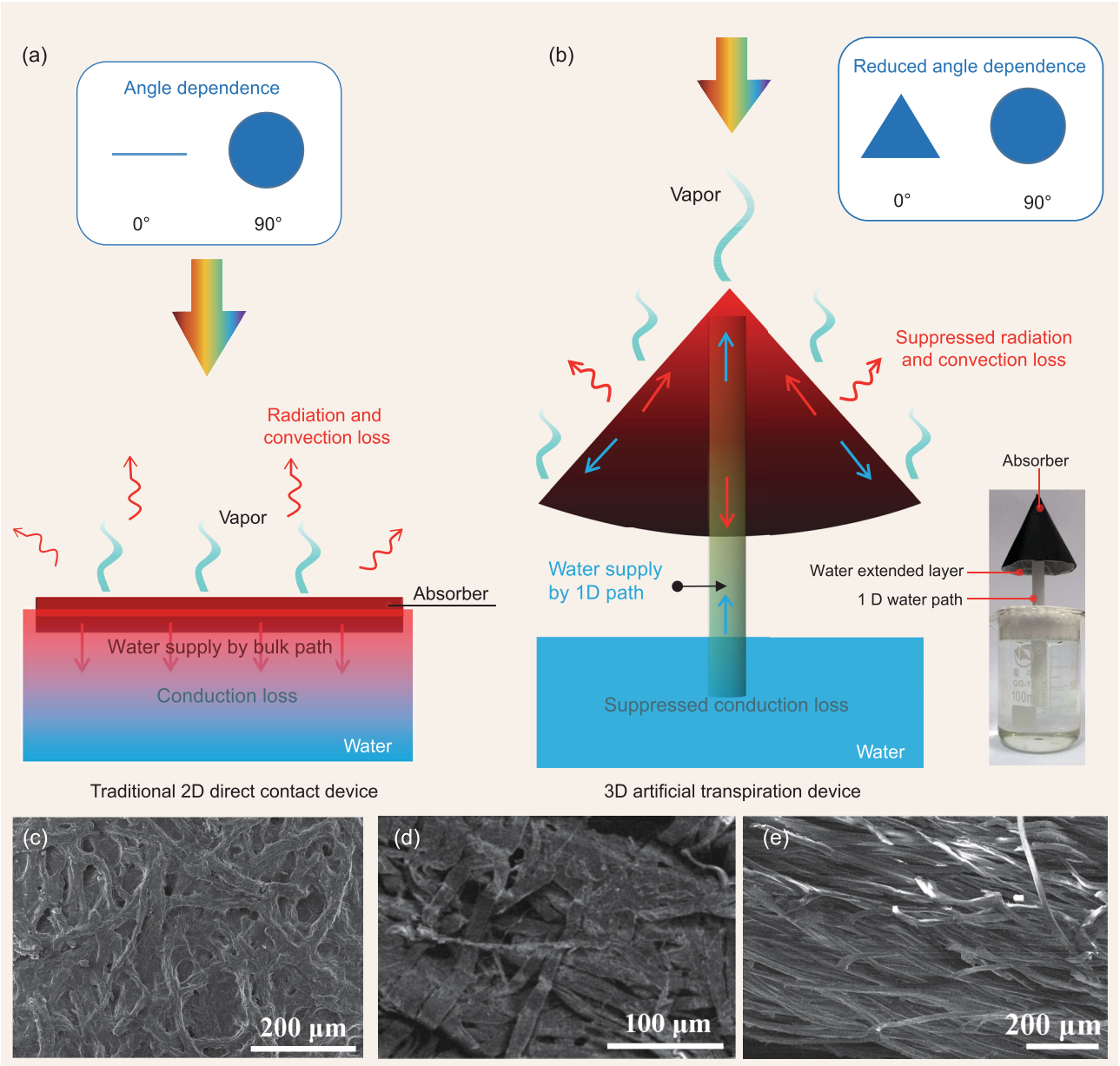

Figure 1. Schematics of different solar steam generators. (**a**) Schematics of traditional 2D solar steam generation with direct water contact. (Here, the conduction loss means the heat from the absorber to bulk water. The convection and radiation loss mean the heat from absorber to environment.) (**b**) Schematics of the 3D artificial transpiration device with suppressed heat loss. (The red straight arrows represent the direction of heat conduction. The red crooked arrows represent the direction of heat convection and radiation. The blue straight arrows represent the direction of water supply.) (**c–e**) The SEM images of the absorber, water extended layer and 1D water path, respectively.

confined 1D water path (a cotton rod is used as an example) by capillary force all the way up to the connection point at the top of a hollow cone absorber (GO film [24–26] with >95% absorption weighted by AM1.5 G, Supplemental S1, available as Supplementary Data at *NSR* online). Water then flows down along the thin side-wall of this cone (details in the Methods section), receiving absorbed solar energy for evaporation to the atmosphere through the pores in the GO film [26] (Fig. 1b).

There are several unique features in these artificial transpiration devices. (i) Combining a 3D cone absorber with a 1D water path, this artificial transpiration device enhances the evaporation area and rate. This lowers the operating temperature, reducing radiation, convection and conduction losses. This pushes solar vapor efficiency to >85%, using only one sun irradiation without extra thermal insulation. (ii) Similarly to plants, 3D artificial transpiration devices can receive light from a wide range of

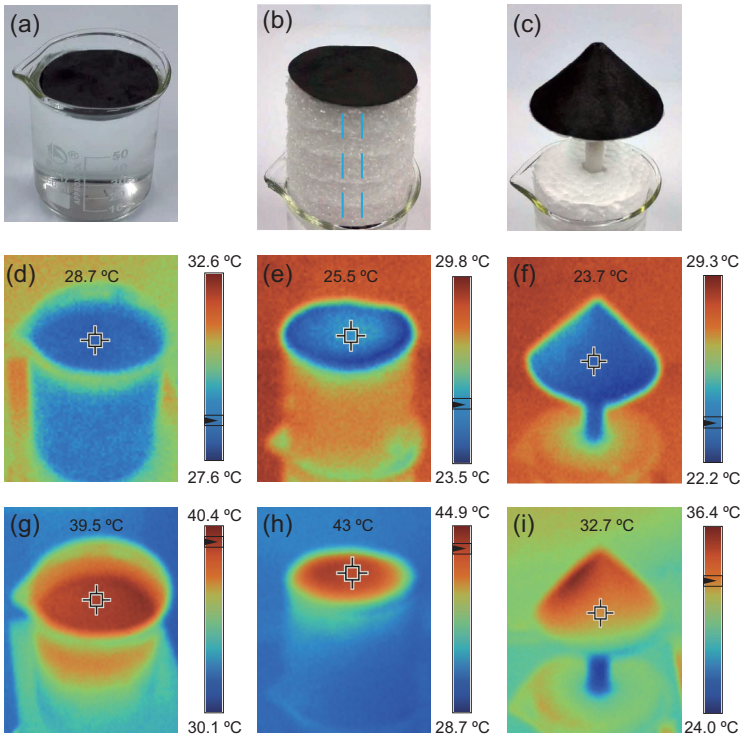

Figure 2. Temperature distributions within different solar steam generators. (**a–c**) The optical images of 2D direct contact, 2D indirect contact (the inserted blue dash line represents the embedded 1D water path) and 3D artificial transpiration devices, respectively. (**d–f**) Temperatures of the GO films in the 2D direct contact, 2D indirect contact and 3D artificial transpiration devices, respectively, before irradiation. (**g–i**) Temperatures of the GO films in the 2D direct contact, 2D indirect contact and 3D artificial transpiration devices, respectively, after 30-min irradiation under one sun. Beakers (without any thermal insulation) are used in this experiment. Ambient temperature is ∼30°C.

angles of incidence, and do not suffer the cosine losses of horizontal 2D receivers. (iii) The artificial transpiration device has a fast thermal response, which reduces the influence of detrimental factors in real applications (such as inconsistent sunlight due to partial cloud cover). All of these features are carefully examined below.

RESULTS AND DISCUSSION

To clearly illustrate these features, our 3D artificial transpiration device is carefully evaluated in comparison with two other devices: 2D absorbers with direct water contact (2D direct contact) and 2D absorbers with 1D water contact (2D indirect contact), as shown in Fig. 2a–c. Without any light illumination, the surface temperature of the 2D direct contact device is maintained at around 28.7°C, with the environment at ∼30°C (Fig. 2d). For comparison, under the same conditions, the temperatures of 2D indirect contact and 3D artificial transpiration devices are 25.5°C and 23.7°C (Fig. 2e and f), respectively, indicating the cooling effect due to the evaporation of water. After 30-min irradiation under one sun, the surface temperatures at the center of the absorbers for 2D direct contact, 2D indirect contact and 3D artificial transpiration become 39.5°C, 43°C and 32.7°C, respectively (Fig. 2g–i). Compared with the 2D direct contact, the 2D indirect contact has higher surface temperature because of suppressed heat conduction due to 1D water contact (more analysis below). While the 3D artificial transpiration device also has suppressed heat conduction, the surface temperature of the absorber is the lowest because of the increased surface area for efficient evaporation (evaporation mechanism in Supplemental S2, available as Supplementary Data at *NSR* online), which lowers radiation and convection losses. According to absorber temperatures measured by infrared radiation (IR) camera (Fig. 2g–i), the radiation losses of 2D direct contact, 2D indirect contact and 3D artificial transpiration devices are estimated to be 7%, 11% and 7%, respectively (more details about calculation in Supplemental S3a and the simulation in Supplemental S4, both available as Supplementary Data at *NSR* online). The convection losses are estimated to be 5%, 9% and 6%, respectively (Supplemental S3b and S4, available as Supplementary Data at *NSR* online). Meanwhile, the conduction loss for 2D direct contact, 2D indirect contact and 3D artificial transpiration were measured to be 43%, 2% and 1%, respectively (Supplemental S3c and S4, available as Supplementary Data at *NSR* online). The minimized conduction loss is also evident by the much reduced temperature of the water beneath the devices over time under illumination (Supplemental S5, available as Supplementary Data at *NSR* online). Our experiments show that, by combining 3D hollow cone absorbers with 1D water paths, the 3D artificial transpiration device can minimize radiation, convection and conduction heat losses.

To systematically evaluate the solar vapor generation efficiency, the evaporation rates are measured by recording the mass change over time under both one sun solar illumination (1 kW/m^2) and dark unilluminated conditions. The various evaporation devices were placed within beakers without any extra thermal insulation (Fig. 3a–c). The evaporation rates of 2D direct contact, 2D indirect contact and 3D artificial transpiration under dark conditions are 0.09 kg/m^{2}h, 0.28 kg/m^{2}h and 0.47 kg/m^{2}h, respectively. The increased water evaporation rate of the 3D artificial transpiration device is attributed to the increased surface area. The evaporation rate under dark conditions is subtracted from all the measured

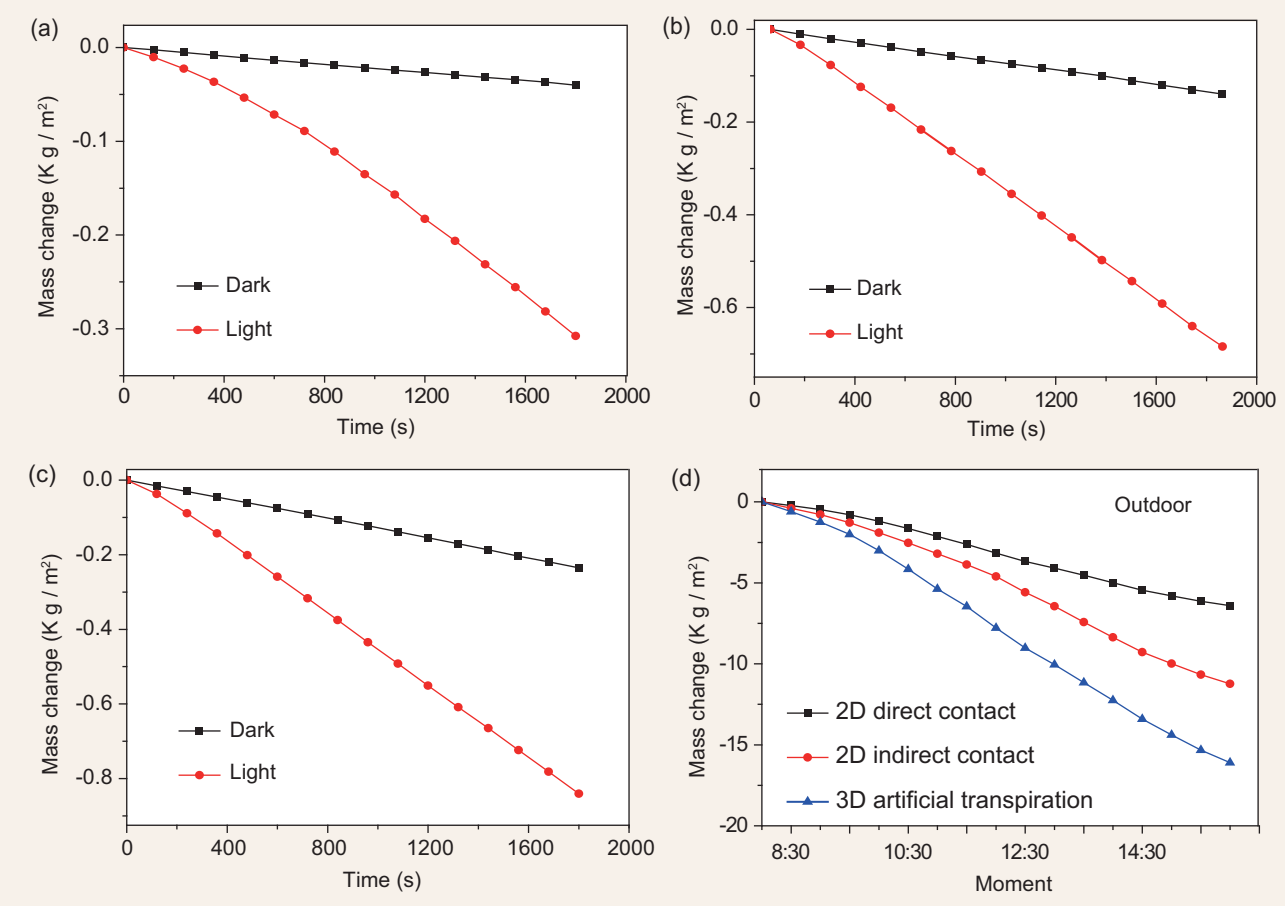

Figure 3. The performance of solar steam generators under solar illumination. (**a**) Mass changes over time with and without illumination using the 2D direct contact device. (**b**) Mass changes over time with and without illumination using the 2D indirect contact device. (**c**) Mass changes over time with and without illumination using the 3D artificial transpiration device. (**d**) Mass changes over time outdoors using the 2D direct contact device, 2D indirect contact device and 3D artificial transpiration device, respectively.

evaporation rates under irradiation to evaluate the solar thermal efficiency. The efficiency formula

$$\eta = \dot{m}\,(Lv + Q)\,/P_{in}$$

is employed for calculating the efficiency(η), in which $\dot{m}$ is the mass flux ($\dot{m} = m_{Light} - m_{Dark}$) kg/m^{2}h, Lv is the latent heat of vaporization of water ($Lv\,(\mathrm{T}) = 1.91846 \times 10^6\,[T/(T-33.91)]^2$ J/kg, where T is the temperature of vaporization) [27], Q is the sensible heat of water of unit mass ($Q = c\,(T_2 - T_1)$ J/kg, where c is the specific heat of water, which can be assumed as a constant (4.2 J/gK), T_2 is the temperature of vaporization and T_1 is the initial temperature of the water) and P_{in} is the incident solar power on the device surface. The solar vapor generation efficiency of the 3D artificial transpiration device can reach 85%, which is higher than values for the 2D indirect contact (76%) and 2D direct contact (49%) devices (more details about heat losses and efficiencies are in Supplemental S2, available as Supplementary Data at *NSR* online). The devices with a 1D water path (2D indirect contact and 3D artificial transpiration) can reach a steady state in much shorter periods, typically after a few hundred seconds (Fig. 3c). This characteristic can reduce the influence of detrimental factors in real applications such as inconsistent sunlight due to partial cloud cover (simulation and calculation shown in Supplemental S6, available as Supplementary Data at *NSR* online). The lumped capacitance model is used to illustrate the benefits of fast thermal performance. The devices with a 1D water path (2D indirect contact and 3D artificial transpiration) reached a steady state quickly due to the low thermal mass of the system. However, in the 2D direct contact device, the device's thermal mass is coupled with the thermal mass of the whole beaker of water.

Another feature in our 3D artificial transpiration device is the ability to collect more sunlight throughout the day, compared with a flat horizontal device. In contrast to the fixed, simulated sun light used in the lab, the sun's sky position is constantly changing.

Furthermore, around 10–50% of the sunlight is diffuse, arriving at the receiver from all directions (about 10 ∼ 20% on sunny days and 50% on cloudy days) [28,29]. Compared with 2D devices for solar vapor generation, our artificial transpiration device with 3D absorption structure performs better in real-world applications due to better light absorption (∼24% improvement, calculation in Supplemental S7, available as Supplementary Data at *NSR* online) from a wide range of incident angles during any period of the day and large dark evaporation (Fig. 3c). As shown in Fig. 3d, the outdoor solar vapor experiment was conducted from 8:00 am to 4:00 pm (the experimental parameters are shown in Supplemental S8, available as Supplementary Data at *NSR* online). The total evaporation of 3D artificial transpiration device is 16.1 Kg/m^2, which is 1.43x that of the 2D indirect contact device and 2.52x that of the 2D direct contact device with the same ground-occupied area. It is clear that the 3D artificial transpiration device has advantages for real-world applications compared with 2D devices. Because of scalable processes (spray-coating [30]), materials and structures (water can be supplied to heights of several meters [31]), single stand-alone 3D artificial transpiration devices can be magnified from several centimeters to several meters, offering higher water output given limited footprint, compared with 2D structures.

As water pollution, especially heavy-metal pollution, has become a pervasive and severe problem worldwide [32–34], several methods such as chemical precipitation, adsorption, ion-exchange, electrochemical treatment and membrane purification have been pursued for effective water treatment [35]. However, further development of these approaches is needed to address issues related to energy consumption, intrinsic costs, second pollution and efficiency. In contrast, solar vapor is a promising solution to these issues. Our 3D artificial transpiration device has high output (Fig. 3c,d), compared with 2D devices, enables effective water treatment through two pathways, producing clean water condensed from vapor and recycling precious heavy metals.

As a demonstration, water treatment performance was evaluated using various solutions of $CuSO_4{\cdot}5H_2O$, $CdSO_4$, $PbCl_2$ and $ZnSO_4$, which have heavy-metal ions (Cu^{2+}, Cd^{2+}, Pb^{2+}, Zn^{2+}). The ion concentrations are carefully tracked by atomic absorption spectroscopy (more experimental details in the Methods section). As shown in Fig. 4a, starting with water with Cu^{2+}, Cd^{2+}, Pb^{2+} and Zn^{2+} concentration as high as 5000 mg/L (5000 times higher than World Health Organization (WHO) drinking-water standards), the extracted water from the condensed steam is pure enough to meet WHO drinking-water standards. It is also confirmed that the effect of decontamination is not dependent on pH values (Fig. 4b). The stable clean-water production performance of the 3D artificial transpiration device over 50 cycles (with 1 hour each cycle) was demonstrated, as shown in Fig. 4c.

Heavy-metal recovery is another important strategy for waste-water treatment, particularly for water contaminated by valuable heavy-metal ions [34,36]. Here, $CuSO_4{\cdot}5H_2O$ (Fig. 4d) and $HAuCl_4{\cdot}4H_2O$ (Supplemental S9, available as Supplementary Data at *NSR* online), common pollutants found in waste water from the electroplating industry, were chosen as examples. When the artificial transpiration device was put in contact with solution of heavy-metal salt, the solutions were wicked up through capillarity to the 3D artificial transpiration devices. Under solar illumination, the heavy-metal salt precipitates. As shown in Fig. 4d, the $CuSO_4{\cdot}5H_2O$ is precipitated on the surface of our device after 5 hours of solar irradiation (note: the $CuSO_4{\cdot}5H_2O$ with 200 g/L was selected as a representative heavy-metal ion contaminant to evaluate the service cycle. However, real electroplating waste water is about 0.02 ∼ 0.1 g/L, and thus the device does not require frequent replacement (expected lifetime of ∼300 days when the concentration is 0.1 g/L and the output is 30 L/m^2d). It is expected that similar approaches can be applied to other heavy-metal ions (such as Pt^{4+}, Cr^{2+}, Ni^{2+}, etc.).

CONCLUSIONS

In summary, we demonstrate a 3D artificial transpiration device with innately minimized radiation, convection and conduction losses which enables over 85% solar vapor efficiency under one sun irradiation without external thermal insulation and optical supporting systems. This approach will fundamentally improve the scalability and economics of solar vapor generation. In the future, the 3D structure design can be optimized to increase storage capacity for heavy-metal salts, to increase device lifetime. To accomplish this, the thickness of the conical GO film could be increased, or the porosity increased. The conical shape could be replaced with different geometries such as north–south-oriented tent-shapes to further improve optical absorption at low incidence angles. Using high-efficiency and low-cost materials, together with scalable fabrication processes, our developed 3D artificial transpiration device enables promising pathways for effective water treatment, recycling valuable heavy metals and purifying contaminated water, and opens up many other possibilities for solar thermal energy harvesting and utilization.

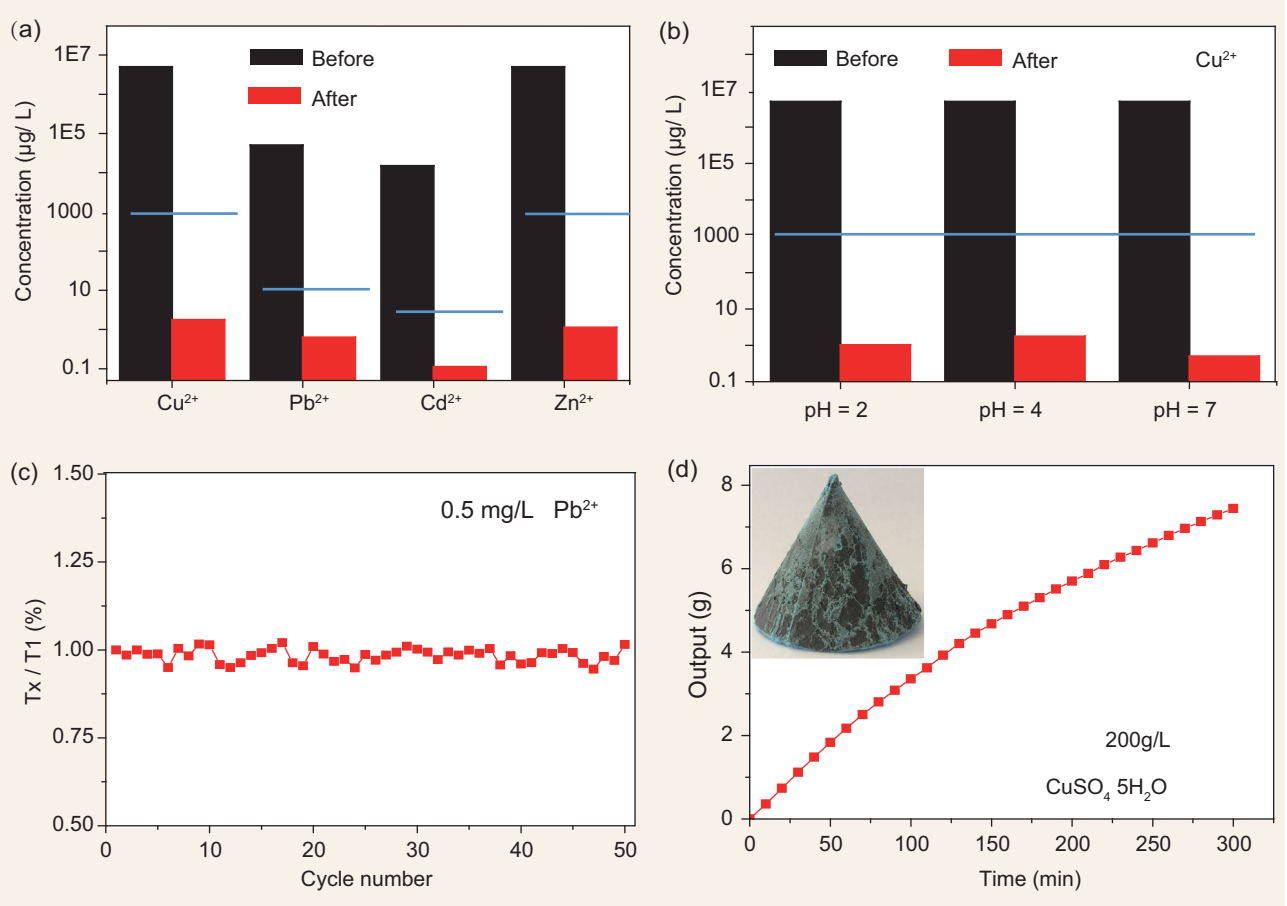

Figure 4. Two pathways of solar waste-water treatment. (**a**) Concentrations of different metal ions before and after treatment. The blue-colored lines refer to the WHO standards for drinkable water. (**b**) Concentrations of Cu^{2+} before and after treatment under different pH conditions. The blue-colored lines refer to the WHO standards for drinkable water. (**c**) Stable cycling performance of the 3D artificial transpiration device for treating Pb^{2+}-contaminated water over 50 cycles, with each cycle sustained over 1 hour (*y*-axis, T_1 means output of purified water in the first cycle and Tx means output of purified water in the X cycle). (**d**) The output of purified water over irradiation time (insert, the optical image of the absorber after 5-h irradiation and recovered $CuSO_4{\cdot}5H_2O$ crystal).

METHODS

Fabrication of 3D artificial transpiration device

Fabrication of GO film: GO was prepared from graphite powder by a modified Hummers' method. GO aqueous solution at a concentrations of 3 mg/mL was added to a commercial airbrush (nozzle diameter of 0.3 mm, Ustar CD-601, Taiwan, China). Spray-coating was performed by toggling the air valve, and the GO solution was atomized into small droplets which were carried by air toward the preheated substrate. Finally, GO films were obtained on filter paper by spray deposition of GO aqueous solution. The GO films (the diameter of the 2D direct contact is 4.5 cm; the diameter of the 2D indirect contact is 4.5 cm; the diameter of the 3D is 4.5 cm and the angulus parietalis is 90°) as absorbers were used in this experiment.

Fabrication of a 1D water supply path for the 2D indirect contact and 3D artificial transpiration structure: as shown in Fig. 1b, a commercial absorbent cotton rod (as a 1D water supply path, diameter: 7 mm, height (above bulk water): 6 cm) was inserted into polystyrene foam for mechanical support, with one end immersed under bulk water and the other end connected to a water extended layer (cellulous paper) under GO film, to ensure the efficient water supply by capillary force.

Characterizations

Morphologies and structures of the absorbent cotton core, water extended layer and GO film were characterized by SEM (Dual-beam FIB 235, FEI Strata). The atomic ratios of carbon to oxygen and the existence of functional groups of GO were characterized using X-ray photoelectron spectroscopy

(XPS, PHI 5000 Versa Probe), equipped with a monochromatic Al Ka X-ray source operated in a residual vacuum of 5×10^{-9} Torr. The absorption of the wet GO film was measured from 200 nm to 2500 nm wavelength using UV/vis spectroscopy (UV-3600, Shimadzu). The thermal images were captured by using a FLUKE Ti 100 infrared camera. The content of heavy-metal ions of purified water was characterized by atomic absorption spectroscopy (AAS, 180-80, Hitachi).

Solar vapor generation and solar waste-water treatment

The 3D artificial transpiration device was floated on solutions in a beaker. The samples were irradiated by a solar simulator (Newport 94043A, Class AAA) with an optical filter for the standard AM 1.5-G spectrum. The temperature of the water surface was recorded by thermocouples (placed on top of the surface of the water), and the temperature of the GO film was monitored using an infrared camera. The weight change was monitored by an electronic analytical scale (FA 2004), real time recorded by computer (with RS-232 serial ports) and then used to determine the evaporation rate of solar vapor generation. The evaporation rate under dark conditions ('dark evaporation') is subtracted from all the measured evaporation rates under the irradiation. $CuSO_4 \cdot 5H_2O$, $CdSO_4$, $PbCl_2$ and $ZnSO_4$ were selected as model heavy-metal ion (Cu^{2+}, Cd^{2+}, Pb^{2+}, Zn^{2+}) contaminants to evaluate clean-water generation performance. All experiments were conducted with dark and light evaporation at the same ambient temperature and humidity.

The collection of purified water: as shown in Supplemental S10 (available as Supplementary Data at *NSR* online), the solar vapor generation device was placed in a double-slope solar still setup (a clean glass plate was used as the roof to allow light to pass through) for steam condensation and purified water collection. Under solar illumination, the steam from the absorber will condense into water when it arrives at the cold chamber wall. Finally, the purified water was obtained.

SUPPLEMENTARY DATA

Supplementary Data are available at *NSR* online.

ACKNOWLEDGEMENT

We acknowledge the micro-fabrication center of National Laboratory of Solid State Microstructures (NLSSM) for technical support. We acknowledge Prof. Gang Chen at MIT for valuable discussions. All authors discussed the results and approved the final version of the manuscript.

FUNDING

This work was supported by the National Basic Research Program of China (973 Program) (2015CB659300), the National Natural Science Foundation of China (11621091 and 11574143), the Natural Science Foundation of Jiangsu Province (BK20150056 and BK20160630), the Postdoctoral Science Foundation of China (2016M601774), the Project Funded by the Priority Academic Program Development of Jiangsu Higher Education Institutions (PAPD) and the Fundamental Research Funds for the Central Universities.

Conflict of interest statement. None declared.

REFERENCES

1. Bae K, Kang G and Cho SK *et al.* Flexible thin-film black gold membranes with ultrabroadband plasmonic nanofocusing for efficient solar vapour generation. *Nat Commun* 2015; **6**: 10103.
2. Tian LM, Luan JY and Liu KK *et al.* Plasmonic biofoam: a versatile optically active material. *Nano Lett* 2016; **16**: 609–16.
3. Zhou L, Tan YL and Ji DX *et al.* Self-assembly of highly efficient, broadband plasmonic absorbers for solar steam generation. *Sci Adv* 2016; **2**: e1501227.
4. Jiang Q, Tian LM and Liu KK *et al.* Bilayered biofoam for highly efficient solar steam generation. *Adv Mater* 2016; **28**: 9234.
5. Wang J, Li YY and Deng L *et al.* High-performance photothermal conversion of narrow-band gap TiO_3 nanoparticles. *Adv Mater* 2016; doi: 10.1002/adma.201603730.
6. Wang YC, Zhang LB and Wang P. Self-floating carbon nanotube membrane on macroporous silica substrate for highly efficient solar-driven interfacial water evaporation. *ACS Sustain Chem Eng* 2016; **4**: 1223–30.
7. Ghasemi H, Ni G and Marconnet AM *et al.* Solar steam generation by heat localization. *Nat Commun* 2014; **5**: 4449.
8. Ito Y, Tanabe Y and Han JH *et al.* Multifunctional porous graphene for high-efficiency steam generation by heat localization. *Adv Mater* 2015; **27**: 4302–7.
9. Ni G, Miljkovica N and Ghasemia H *et al.* Volumetric solar heating of nanofluids for direct vapor generation. *Nano Energy* 2015; **17**: 290–301.
10. Ni G, Li G and Boriskina SV *et al.* Steam generation under one sun enabled by a floating structure with thermal concentration. *Nat Energy* 2016; doi: 10.1038/nenergy.2016.126.
11. Sajadi SM, Farokhnia N and Irajizad P *et al.* Flexible artificially-networked structure for ambient/high pressure solar steam generation. *J Mater Chem A* 2016; **4**: 4700–5.
12. Zielinski MS, Choi JW and Grange TL *et al.* Hollow mesoporous plasmonic nanoshells for enhanced solar vapor generation. *Nano Lett* 2016; **16**: 2159–67.
13. Hu XZ, Xu WC and Zhou L *et al.* Tailoring graphene oxide-based aerogels for efficient solar steam generation under one sun. *Adv Mater* 2016; doi: 10.1002/adma.201604031.

14. Jin HC, Lin GP and Bai LZ *et al.* Steam generation in a nanoparticle-based solar receiver. *Nano Energy* 2016; **28**: 397–406.
15. Zhou L, Tan YL and Wang JY *et al.* 3D self-assembly of aluminium nanoparticles for plasmon-enhanced solar desalination. *Nat Photon* 2016; **10**: 393–8.
16. Neuman O, Ferontic C and Neumannc AD *et al.* Compact solar autoclave based on steam generation using broadband light-harvesting nanoparticles. *PNAS* 2013; **110**: 11677–81.
17. Liu Y, Yu ST and Feng R *et al.* A bioinspired, reusable, paper-based system for high-performance large-scale evaporation. *Adv Mater* 2015; **27**: 2768–74.
18. Gao MM, Connora PKN and Ho GW. Plasmonic photothermic directed broadband sunlight harnessing for seawater catalysis and desalination. *Energy Environ Sci* 2016; **9**: 3151–60.
19. Zhang L, Tang B and Wu J *et al.* Hydrophobic light-to-heat conversion membranes with self-healing ability for interfacial solar heating. *Adv Mater* 2015; **27**: 4889–94.
20. Wang XQ, Ou G and Wang N *et al.* Graphene-based recyclable photo-absorbers for high-efficiency seawater desalination. *ACS Appl Mater Inter* 2016; **8**: 9194—9.
21. Li XQ, Xu WC and Tang MY *et al.* Graphene oxide-based efficient and scalable solar desalination under one sun with a confined two-dimensional water path. *PNAS* 2016; **113**: 13953–8.
22. Mcelrone AJ, Choat B and Gambetta GA *et al.* Water uptake and transport in vascular plants. *Nature Education Knowledge* 2013; **4**: 6–12.
23. Tyree M and Ewers FW. The hydraulic architecture of trees and other woody plants. *New Phytol* 1991; **119**: 345–60.
24. Park S and Ruoff RS. Chemical methods for the production of graphenes. *Nat Nanotechnol* 2009; **4**: 217–24.
25. Hummers WS and Offeman RE. Preparation of graphitic oxide. *J Am Chem Soc* 1958; **80**: 1339.
26. Nair RR, Wu HA and Jayaram PN *et al.* Unimpeded permeation of water through helium-leak-tight graphene-based membranes. *Science* 2012; **335**: 442–4.
27. Sellers BH. A new formula for latent heat of vaporization of water as a function of temperature. *Quart J R Met Soc* 1984; **110**: 1186–90.
28. Liu BY and Jordan RC. The interrelationship and characteristic distribution of direct, diffuse and total solar radiation. *Sol Energy* 1960; **4**: 1–19.
29. Green MA. Solar cells: operating principles, technology, and system applications. Englewood Cliffs: Prentice-Hall, 1982.
30. Li XQ, Zhang D and Yang C *et al.* Direct and efficient preparation of graphene transparent conductive films on flexible polycarbonate substrate by spray-coating. *J Nanosci Nanotechnol* 2015; **15**: 9500–8.
31. Zhang XT, Kan WM and Jiang HQ *et al.* Capillary-driven low grade heat desalination. *Desalination* 2017; **410**: 10–8.
32. Shannon MA, Bohn PW and Elimelech M *et al.* Science and technology for water purification in the coming decades. *Nature* 2008; **452**: 301–10.
33. Duruibe JO, Ogwuegbu MO and Egwurugwu JN. Heavy metal pollution and human biotoxic effects. *Int J Phys Sci* 2007; **2**: 112–8.
34. Bolisetty S and Mezzenga R. Amyloid-carbon hybrid membranes for universal water purification. *Nat Nanotech* 2016; **11**: 365–71.
35. Fu F and Wang Q. Removal of heavy metal ions from wastewaters: a review. *J Environ Manage* 2011; **92**: 407–18.
36. Wang HM and Ren ZJ. Bioelectrochemical metal recovery from wastewater: A review. *Water Res* 2014; **66**: 219–32.